

Stripe antiferromagnetism in van der Waals metal HoTe_3 decoupled from charge density wave order

Weiyi Yun,¹ Ryota Nakano,¹ Ryo Misawa,¹ Rinsuke Yamada,¹ Shun Akatsuka,¹
Yoshichika Ōnuki,² Priya Ranjan Baral,¹ Hiraku Saitoh,³ Ryoji Kiyonagi,⁴ Takashi
Ohhara,⁴ Taro Nakajima,³ Taka-hisa Arima,^{2,5} and Max Hirschberger^{1,2,*}

¹*Department of Applied Physics and Quantum-Phase Electronics Center (QPEC),
The University of Tokyo, Bunkyo, Tokyo 113-8656, Japan*

²*RIKEN Center for Emergent Matter Science (CEMS), Wako, Saitama 351-0198, Japan*

³*The Institute for Solid State Physics, The University of Tokyo, Kashiwa 277-8581, Japan*

⁴*J-PARC Center, Japan Atomic Energy Agency, Tokai 319-1106, Japan*

⁵*Department of Advanced Materials Science, The University of Tokyo, Kashiwa, Chiba 277-8561, Japan*

(Dated: February 19, 2026)

The $R\text{Te}_3$ (R = rare earth) family of layered van der Waals (vdW) compounds hosts coexisting magnetic and charge density wave (CDW) orders, yet the interplay between these degrees of freedom remains little explored. Combining polarized and unpolarized neutron diffraction on single-crystal HoTe_3 , we identify two distinct antiferromagnetic (AFM) phases, both exhibiting a collinear $\uparrow\uparrow\downarrow\downarrow$ motif within individual vdW layers. The two phases are distinguished by the vdW stacking of magnetic layers: ferromagnetic (FM) stacking in the higher-temperature AFM-II phase, here termed “vertical-stripe”, and AFM stacking in the AFM-I ground state, here termed “tilted-stripe”; the two phases have propagation vectors $\mathbf{q}_{m2} = (0.48, 0, 0)$ and $\mathbf{q}_{m1} = (0.5, 0.5, 0)$, respectively. In contrast to the CDW-driven exotic magnetism in DyTe_3 , TbTe_3 , and GdTe_3 , we find no evidence for coupling between magnetism and CDW in HoTe_3 . The relative alignment between AFM and CDW propagation vectors, as well as single-ion anisotropy, are likely essential for generating coupled spin/charge orders in layered vdW systems.

Introduction – Rare-earth tritellurides ($R\text{Te}_3$) are quasi-two-dimensional, layered van der Waals (vdW) compounds that exhibit rich electronic and magnetic phenomena. The $R\text{Te}_3$ are known to host robust charge density waves (CDWs) [1–13] related to Fermi surface nesting between nearly parallel sheets derived from $\text{Te-}5p$ orbitals [9, 11, 14–16]. In $R\text{Te}_3$ with heavy rare earths, the CDW order is a complex superposition of two charge modulations with orthogonal propagation directions, as depicted in Fig. 1(c) by the gray surface, with CDW-1 and CDW-2 propagating along the crystallographic c - and a -axes, respectively. This complex checkerboard pattern of charge (termed double- \mathbf{q} CDW order) is highly sensitive to the lattice volume as controlled by the rare earth R in $R\text{Te}_3$ [10]. Antiferromagnetic order [17–21] is present in the $R\text{Te}_3$ at low temperature, and superconductivity can be induced via external pressure [22, 23]. The intricate coupling among charge, orbital, lattice and spin degrees of freedom makes $R\text{Te}_3$ an ideal platform for exploring correlation phenomena in low-dimensional systems, where atomically flat surfaces can be prepared by exfoliation for advanced experimental techniques. There is also a prospect for vdW heterostructure engineering using this class of materials [18].

$R\text{Te}_3$ compounds crystallize in an orthorhombic structure (space group $Cmcm$, No. 63), as shown in Fig. 1(a). The crystal lattice consists of bilayers of highly metallic Te square nets separated by covalently bonded R -Te slabs, with the stacking direction corresponding to the orthorhombic b -axis. Here, we focus on two representative

members of the family: Fig. 1(b) shows the coupled spin and charge order of DyTe_3 , with a predominantly unidirectional charge modulation (CDW-1) [24]. A collinear $\uparrow\uparrow\downarrow\downarrow$ magnetic structure couples to the CDW, stabilizing an exotic helimagnetic cone phase [25]. Similar coupling between CDW-1 and AFM order has been reported in GdTe_3 [18] and TbTe_3 shows a complex sequence of magnetic transitions with coupled CDW and AFM order [26, 27]. The detailed spin patterns of TbTe_3 and GdTe_3 remain to be solved.

In this Letter, we combine neutron diffraction and magnetization measurements to determine the magnetic phases and spin textures of HoTe_3 in presence of a strong double- \mathbf{q} order parameter. We identify collinear $\uparrow\uparrow\downarrow\downarrow$ type AFM order within individual vdW layers, as depicted in Fig. 1(c). Our magnetic structure analysis is based on symmetry considerations and full refinement of the magnetic structure. Since no evidence is found for cross-talk between CDW-2 and AFM order in HoTe_3 , we suggest that the strong double- \mathbf{q} CDW order parameter is detrimental for coupling charge and spin order.

Results – The magnetic phase diagram of HoTe_3 in the B - T plane [Fig. 1(d)] reveals two successive antiferromagnetic phases, AFM-I and AFM-II. The zero-field phase transition between these phases is clearly visible in the temperature dependence of the magnetic scattering intensity [Fig. 1(e)]. Focusing on the ground state AFM-I, characterized by the magnetic propagation vector $\mathbf{q}_{m1} = (0.5, 0.5, 0)$, we combine polarized neutron scattering with symmetry analysis to identify its mag-

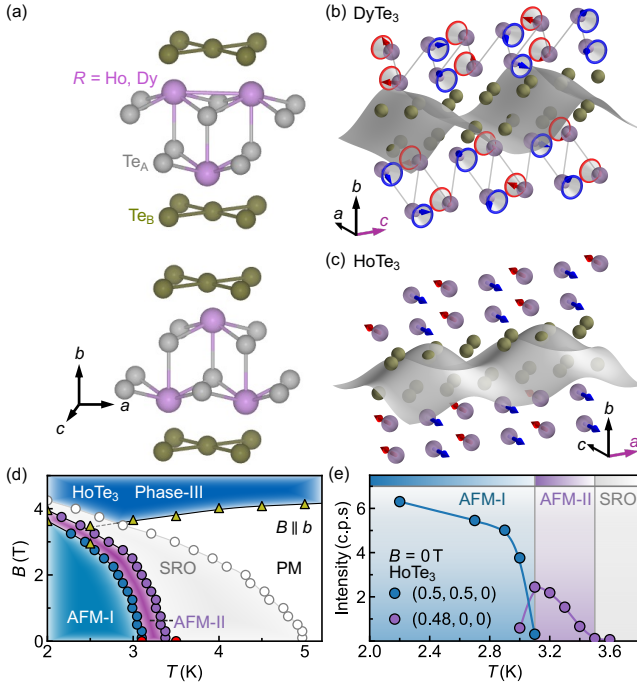


FIG. 1. (color online). Magnetism in $R\text{Te}_3$ ($R = \text{Ho}, \text{Dy}$) with charge density wave (CDW) order. (a) Orthorhombic crystal structure with space group $Cmc21$ (No. 63) in layered HoTe_3 , showing covalently bonded $\text{Ho}-\text{Te}_A$ bilayers and conducting Te_B square nets [28]. Note that the b -axis is perpendicular to the vdW layers. (b) Charge order in DyTe_3 is predominantly unidirectional along c . Its conical magnetic texture is modulated along the c -axis through coupling to the CDW-1. (c) HoTe_3 has a more strongly double- q character of the CDW, with two propagation vectors. Its AFM-I ground state has moments parallel to the c -axis and is independent of the double q -CDW. Te_A atoms and CDW-induced lattice distortions are not depicted. (d) B - T magnetic phase diagram of HoTe_3 with field applied along the b -axis. Phase boundaries are determined from magnetization measurements. The light gray region between the PM and AFM-II phases hosts short-range magnetic order (SRO). (e) Temperature dependence of magnetic reflection intensities in HoTe_3 corresponding to the AFM-I and AFM-II propagation vectors, measured using a triple-axis diffractometer at JRR-3 in zero magnetic field.

netic structure. Our results reveal an Ising-like, alternating tilted-stripe spin texture belonging to the P_a2_1/m magnetic space group, as established by the experimental evidence and symmetry constraints discussed below. The magnetic structure of AFM-II – also collinear $\uparrow\uparrow\downarrow\downarrow$ in a single layer, but layers stacked ferromagnetically – is solved in the Supplementary Information [29] and discussed at the end of the Results section.

We determined the magnetic structure of the AFM-I phase using polarized neutron scattering in the geometry shown in Fig. 2(a). The neutron spin quantization axis was aligned along the crystallographic c -axis, with the scattering plane defined as $hk0$. In this configuration, the non-spin-flip (NSF) and spin-flip (SF) channels

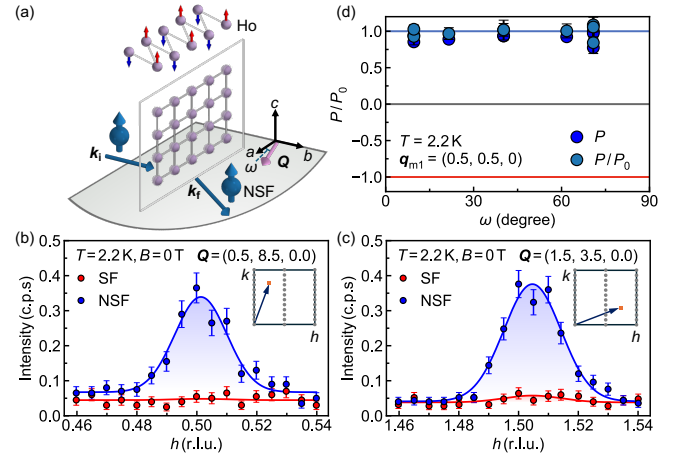


FIG. 2. (color online). Polarized neutron scattering in phase AFM-I of HoTe_3 . (a) The incoming and outgoing wavevectors of the neutron beam, k_i and k_f , span the $hk0$ scattering plane (gray). The total momentum transfer is Q . In the Ho sublattice, moments are collinear along the c -axis (perpendicular to the scattering plane), yielding finite non-spin flip (NSF) and zero spin-flip (SF) scattering intensity. Spin directions of polarized neutrons are shown as blue balls with arrows. (b,c) h -scans at $Q = (0.5, 8.5, 0)$ and $(1.5, 3.5, 0)$. Only NSF scattering is observed. Insets: schematic of Q in the scattering plane. (d) Flipping ratio $P = (I_{\text{NSF}} - I_{\text{SF}})/(I_{\text{NSF}} + I_{\text{SF}})$ at $T = 2.2$ K for magnetic reflections lying in the scattering plane $hk0$, measured as a function of ω , the angle between each reflection's momentum transfer Q and the a -axis ($h00$). P is normalized to P_0 to account for imperfect beam polarization (see text). When all points are on the red (blue) line, the moments are fully parallel (fully perpendicular) to the scattering plane.

selectively probe magnetic moment components parallel and perpendicular to the c -axis, respectively. Neutron scattering is sensitive only to $M^\perp(Q)$, the magnetization component perpendicular to the scattering vector Q . In our geometry, $M^\perp(Q)$ is further resolved into NSF and SF channels. Representative h -scans across magnetic Bragg peaks [Fig. 2(b,c)] show intensity exclusively in the NSF channel. The absence of SF scattering at all observed reflections is quantified by the flipping ratio P , shown and defined in Fig. 2(d). The normalized flipping ratio P/P_0 for all observed reflections in the $hk0$ scattering plane is close to unity, indicating that the Ho^{3+} moments have no detectable components within the $hk0$ plane. Here, P_0 is the reference flipping ratio measured on a strong nuclear (non-magnetic) reflection to account for the imperfect polarization of the incident neutron beam and the analyzer efficiency. We therefore identify the AFM-I phase in HoTe_3 as an Ising-like collinear antiferromagnet with moments aligned along the c -axis.

We use symmetry analysis to identify likely magnetic structure models for the AFM-I phase of HoTe_3 , before comparing these models to unpolarized neutron diffraction data. We determine the highest symmetry sub-

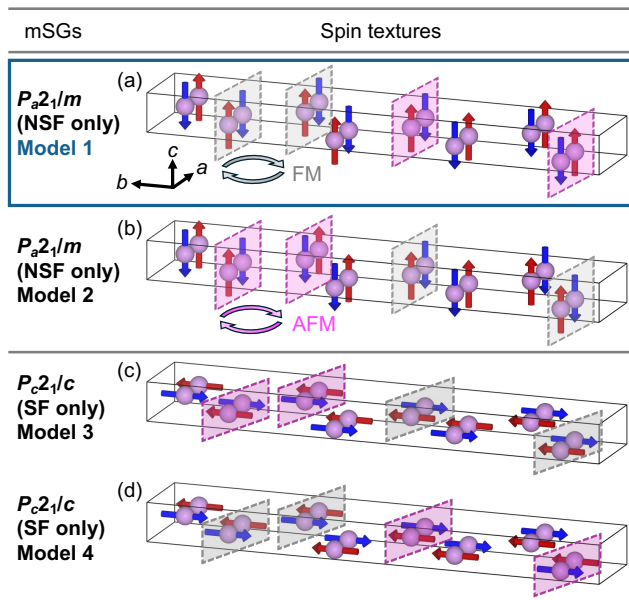


FIG. 3. (color online). Symmetry analysis for phase AFM-I. We show the highest-symmetry magnetic subgroups (mSGs) of the paramagnetic space group $Cmcm1'$ and the corresponding candidate spin textures. (a,b) Magnetic structures in the P_a2_1/m mSG exhibit Ising-like collinear AFM order along the c -axis, consistent with polarized neutron scattering in Fig. 2. (c,d) Magnetic structures in the P_c2_1/c mSG have their moments perpendicular to c , inconsistent with polarized neutron scattering. In each mSG, the Ho atoms at the Wyckoff $4c$ positions are divided into two sets, termed inner and outer set, which are separated by interlayer spacings of approximately $b/3$ and $2b/3$, respectively. In Model 1 (Model 2), the outer (magenta) and inner (gray) Ho sets are AFM (FM) and FM (AFM) coupled, respectively. The structures (c) and (d) can be discussed on the same grounds. Only Model 1 [blue box in (a)] is consistent with the analysis in Fig. 4.

group of the paramagnetic space group $Cmcm1'$ (maximal magnetic subgroup). The analysis is constrained by (i) the Ho^{3+} ions occupying the $4c$ Wyckoff positions and (ii) the magnetic propagation vector $\mathbf{q}_{m1} = (0.5, 0.5, 0)$, which restricts the possible symmetries to two candidate mSGs (Fig. 3). These candidates are distinguished by their magnetic anisotropy: P_a2_1/m enforces an Ising-like magnetic anisotropy with moments aligned along the c -axis, whereas P_c2_1/c requires an XY -like magnetic anisotropy. Polarized neutron scattering uniquely selects P_a2_1/m as the correct mSG, since magnetic reflections with \mathbf{Q} in the $hk0$ plane appear exclusively in the NSF channel. Consequently, two symmetry-allowed magnetic structures within P_a2_1/m remain, as illustrated in Figs. 3(a) and 3(b).

To distinguish between these remaining candidates and also to determine the magnetic domain populations, we performed time-of-flight Laue neutron diffraction using the SENJU diffractometer at J-PARC [Fig. 4(a)].

The measured magnetic reflection pattern [Fig. 4(b)] exhibits a pronounced suppression of intensity along the $(0k0)$ direction, indicating a quasi-extinction behavior that places a stringent constraint on the magnetic structure factor. Considering scattering vectors of the form $\mathbf{Q} = (h', k', l) = \mathbf{G} + \mathbf{q}_{m1}$, where $\mathbf{G} = (h, k, l)$ is a reciprocal lattice vector, and evaluating the structure factor for Model 1 shown in Fig. 3(a), as detailed in the Supplemental Material, we calculate that suppressed reflections satisfy

$$k' = k + \frac{1}{2} = \frac{3n}{2}, \quad n \in \mathbb{Z}, n \text{ odd}, \quad (1)$$

when $l = 0$. For example, the intensity is predicted to be suppressed at $k = 3/2, 9/2, \dots$ as observed experimentally in Fig. 4(b). Models 2-4 cannot explain these suppressed intensity patterns [29] and we thus conclude that the AFM-I phase in HoTe_3 exhibits an alternating tilted-stripe antiferromagnetic structure, illustrated in Fig. 4(c). The construction of AFM-I's spin pattern based on symmetry is detailed in the Supplemental Material.

To quantitatively assess the consistency between the proposed model and the experimental data, we performed magnetic structure refinement, treating the relative population of domains depicted in Fig. 4(c) as the sole adjustable parameter [29]. Figure 4(d) shows the optimal refinement, which produces a population ratio of 48.1 : 51.9 between two magnetic domains related a mirror plane perpendicular to the a -axis. The refined Ho^{3+} moment, $7.89 \mu_B$ per holmium, is reduced from the free-ion value of $10 \mu_B/\text{Ho}$. We note that, at the experimental $T = 1.5 \text{ K}$ ($T/T_{N1} \approx 0.48$), the system remains close to the critical temperature. We expect the ordered moment to approach the free-ion value at zero temperature.

For phase AFM-II, polarized neutron scattering experiments, detailed in the Supplemental Material, again show a flipping ratio $P/P_0 = 1$ for reflections in the $hk0$ plane, indicating that the Ho moments are collinear along the crystallographic c -axis. The magnetic propagation vector $\mathbf{q}_{m2} = (0.48, 0, 0)$ corresponds to ferromagnetic stacking along the c -axis, preserving the c -mirror symmetry of the $Cmcm1'$ paramagnetic space group. Following a similar symmetry analysis as for AFM-I, we identify two candidate mSGs for AFM-II, P_cnma and P_abcm , both of which preserve the c -mirror. Our magnetic structure refinement identifies P_cnma as the mSG of the AFM-II phase. Under the symmetry constraints imposed by the P_cnma magnetic space group, the AFM-II spin texture adopts an Ising-like horizontal-stripe pattern [29].

Conclusions – In summary, polarized neutron scattering reveals the magnetic symmetry of the commensurate AFM-I phase in HoTe_3 to be the magnetic space group P_a2_1/m . By combining the observed suppression pattern with magnetic structure refinements, we establish that AFM-I is an Ising-like collinear antiferromagnet

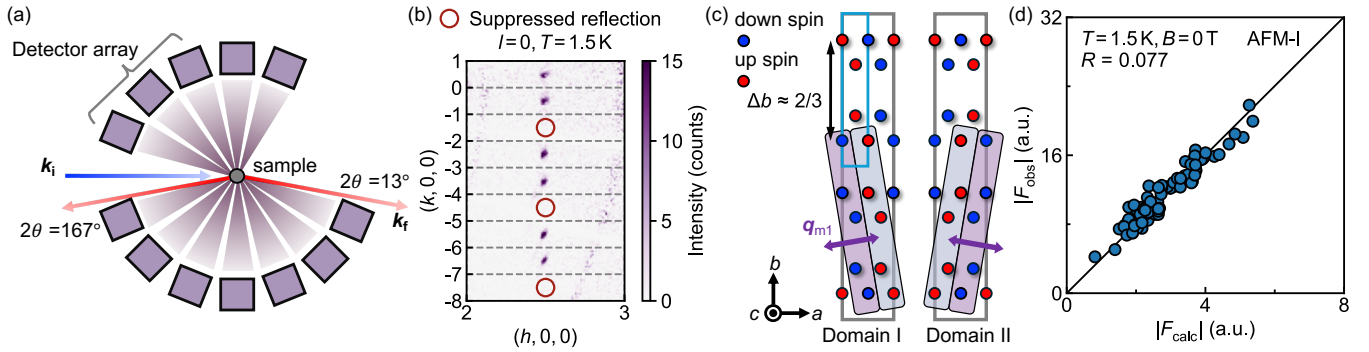


FIG. 4. (color online) Refinement of the magnetic structure in phase AFM-I of HoTe_3 . (a) Geometry of SENJU, a time-of-flight (TOF) Laue diffractometer at J-PARC. Red and blue arrows indicate the ingoing and outgoing neutron wavevectors, \mathbf{k}_i and \mathbf{k}_f . (b) Reconstructed RSM in the $hk0$ plane at $T = 1.5$ K. In AFM-I, there is a pronounced suppression of intensity at $k = -3/2, -9/2, -15/2$ when $l = 0$, consistent with Eq. (1). (c) Two domains of Model 1 for AFM-I, showing alternating tilted-stripe spin textures. Only Ho sites are shown. The gray box indicates the conventional magnetic unit cell, four times larger than the conventional crystallographic unit cell (blue box). Moments align along the c -axis with propagation vector \mathbf{q}_{m1} (purple arrow). The tilted grey and violet boxes with round edges are guides to the eye, indicating planes of parallel spins – i.e., spin stripes. (d) Magnetic refinement of unpolarized neutron intensity using Model 1. F_{obs} , F_{calc} and R denote observed and calculated magnetic structure factors, as well as the agreement factor.

characterized by a tilted-stripe texture. In this configuration, individual layers of Ho^{3+} ions adapt an $\uparrow\uparrow\downarrow\downarrow$ pattern along zigzag chains, and along the b -axis, the closest neighbors across the metallic tellurium layer (distance about $1/3$ of the lattice constant b) are coupled ferromagnetically; c.f. Fig. 4(c). In contrast, the Ho^{3+} ions stacked at a distance $2b/3$ are stacked antiferromagnetically, resulting in a tilted stripe state with collinear spin texture and ordering vector $\mathbf{q}_{m1} = (0.5, 0.5, 0)$. The incommensurate AFM-II phase ($\mathbf{q}_{m2} = 0.48, 0, 0$) similarly adopts an Ising-like horizontal-stripe motif with $\uparrow\uparrow\downarrow\downarrow$ in individual zigzag chain and ferroic stacking for holmium atoms at a distance of $b/3$ along the stacking direction. Here however, the stacking at a distance of $2b/3$ is also ferroic, so that the overall spin texture corresponds to a vertical stripe state [29].

In contrast to the XY -like anisotropy in light $R\text{Te}_3$ members [30], HoTe_3 exhibits robust Ising-like magnetic anisotropy in both AFM phases. In DyTe_3 , the coupled spin-charge order is manifested by the presence of coupled reflections $\mathbf{q}_{\text{CDW}} \pm \mathbf{q}_{\text{AF}}$ in the magnetic diffraction pattern, where $\mathbf{q}_{\text{CDW}} = (0, 0, 0.3)$ and $\mathbf{q}_{\text{AF}} = (0, 0.5, 0.5)$ are the primary propagation vectors of the charge order and the antiferromagnetic texture, respectively. The absence of such coupling in HoTe_3 is distinct from the behavior in DyTe_3 , GdTe_3 , and TbTe_3 , pointing towards a possible role of double- \mathbf{q} charge order in suppressing complex magnetic states in the $R\text{Te}_3$. The shift of the propagation vector from the c -axis in DyTe_3 and to the a -axis in HoTe_3 may also contribute to decoupling the spin and charge orders in HoTe_3 . Our work suggests a systematic evolution of coupled spin and charge orders across the $R\text{Te}_3$ series, stemming from lanthanide-controlled volume changes to the charge density wave

patterns.

Acknowledgements

In this research, we used the ARIM-mdx data system [31]. This work was supported by JSPS KAKENHI Grant Nos. JP24H01607, JP25K17336, and JP24H01604. This work was partially supported by the Japan Science and Technology Agency via JST CREST Grant Number JPMJCR20T1 (Japan), JST FOREST (JPMJFR2238), and JST PRESTO JPMJPR259A. It was also supported by Japan Science and Technology Agency (JST) as part of Adopting Sustainable Partnerships for Innovative Research Ecosystem (ASPIRE), Grant Number JPMJAP2426.

* hirschberger@ap.t.u-tokyo.ac.jp

- [1] V. Brouet, W. Yang, X. Zhou, Z. Hussain, N. Ru, K. Shin, I. Fisher, and Z. Shen, Fermi Surface Reconstruction in the CDW State of CeTe_3 Observed by Photoemission, *Phys. Rev. Lett.* **93**, 126405 (2004).
- [2] P. Walmsley, S. Aeschlimann, J. Straquadine, P. Giraldo-Gallo, S. Riggs, M. Chan, R. McDonald, and I. Fisher, Magnetic breakdown and charge density wave formation: A quantum oscillation study of the rare-earth tritellurides, *Phys. Rev. B* **102**, 045150 (2020).
- [3] A. Kogar, A. Zong, P. E. Dolgirev, X. Shen, J. Straquadine, Y.-Q. Bie, X. Wang, T. Rohwer, I.-C. Tung, Y. Yang, R. Li, J. Yang, S. Weathersby, S. Park, M. E. Kozina, E. J. Sie, H. Wen, P. Jarillo-Herrero, I. R. Fisher, X. Wang, and N. Gedik, Light-induced charge density wave in LaTe_3 , *Nat. Phys.* **16**, 159 (2020).
- [4] L. Rettig, R. Cortés, J.-H. Chu, I. Fisher, F. Schmitt,

- R. Moore, Z.-X. Shen, P. Kirchmann, M. Wolf, and U. Bovensiepen, Persistent order due to transiently enhanced nesting in an electronically excited charge density wave, *Nat. Commun.* **7**, 10459 (2016).
- [5] F. Schmitt, P. S. Kirchmann, U. Bovensiepen, R. G. Moore, L. Rettig, M. Krenz, J.-H. Chu, N. Ru, L. Perfetti, D. H. Lu, M. Wolf, I. R. Fisher, and Z.-X. Shen, Transient Electronic Structure and Melting of a Charge Density Wave in TbTe_3 , *Science* **321**, 1649 (2008).
- [6] A. Chikina, H. Lund, M. Bianchi, D. Curcio, K. J. Dalggaard, M. Bremholm, S. Lei, R. Singha, L. M. Schoop, and P. Hofmann, Charge density wave generated Fermi surfaces in NdTe_3 , *Phys. Rev. B* **107**, L161103 (2023).
- [7] K. Yumigeta, Y. Qin, H. Li, M. Blei, Y. Attarde, C. Kopas, and S. Tongay, Advances in rare-earth tritelluride quantum materials: Structure, properties, and synthesis, *Adv. Sci.* **8**, 2004762 (2021).
- [8] B. F. Hu, B. Cheng, R. H. Yuan, T. Dong, and N. L. Wang, Coexistence and competition of multiple charge-density-wave orders in rare-earth tritellurides, *Phys. Rev. B* **90**, 085105 (2014).
- [9] V. Brouet, W. L. Yang, X. J. Zhou, Z. Hussain, R. G. Moore, R. He, D. H. Lu, Z. X. Shen, J. Laverock, S. B. Dugdale, N. Ru, and I. R. Fisher, Angle-resolved photoemission study of the evolution of band structure and charge density wave properties in $R\text{Te}_3$ ($R = \text{Y, La, Ce, Sm, Gd, Tb, and Dy}$), *Phys. Rev. B* **77**, 235104 (2008).
- [10] N. Ru, J.-H. Chu, and I. Fisher, Magnetic properties of the charge density wave compounds $R\text{Te}_3$ ($R = \text{Y, La, Ce, Pr, Nd, Sm, Gd, Tb, Dy, Ho, Er, and Tm}$), *Phys. Rev. B* **78**, 012410 (2008).
- [11] N. Ru, C. L. Condon, G. Y. Margulis, K. Y. Shin, J. Laverock, S. B. Dugdale, M. F. Toney, and I. R. Fisher, Effect of chemical pressure on the charge density wave transition in rare-earth tritellurides $R\text{Te}_3$, *Phys. Rev. B* **77**, 035114 (2008).
- [12] S. Seong, H. Kim, K. Kim, B. Min, Y. S. Kwon, S. W. Han, B.-G. Park, R. Stania, Y. Seo, and J.-S. Kang, Angle-resolved photoemission spectroscopy study of a system with a double charge density wave transition: ErTe_3 , *Phys. Rev. B* **104**, 195153 (2021).
- [13] C. Malliakas, S. J. Billinge, H. J. Kim, and M. G. Kanatzidis, Square Nets of Tellurium: Rare-Earth Dependent Variation in the Charge-Density Wave of RETe_3 ($\text{RE} = \text{Rare-Earth Element}$), *J. Am. Chem. Soc.* **127**, 6510 (2005).
- [14] R. G. Moore, V. Brouet, R. He, D. H. Lu, N. Ru, J.-H. Chu, I. R. Fisher, and Z.-X. Shen, Fermi surface evolution across multiple charge density wave transitions in ErTe_3 , *Phys. Rev. B* **81**, 073102 (2010).
- [15] J.-S. Kang, S. Seong, E. Lee, Y. S. Kwon, K. Kim, J. Kim, H. Kim, and B. Min, Distinct charge density wave instabilities in PrTe_n ($n = 2, 3$) and ErTe_3 investigated via ARPES and XAS, *Phys. Rev. Mater.* **8**, 080301 (2024).
- [16] E. Lee, D. H. Kim, H. W. Kim, J. D. Denlinger, H. Kim, J. Kim, K. Kim, B. I. Min, B. H. Min, Y. S. Kwon, and J.-S. Kang, The 7×1 Fermi Surface Reconstruction in a Two-dimensional f -electron Charge Density Wave System: PrTe_3 , *Sci. Rep.* **6**, 30318 (2016).
- [17] J. S. Liu, S. C. Huan, Z. H. Liu, W. L. Liu, Z. T. Liu, X. L. Lu, Z. Huang, Z. C. Jiang, X. Wang, N. Yu, Z. Q. Zou, Y. F. Guo, and D. W. Shen, Electronic structure of the high-mobility two-dimensional antiferromagnetic metal GdTe_3 , *Phys. Rev. Mater.* **4**, 114005 (2020).
- [18] S. Lei, J. Lin, Y. Jia, M. Gray, A. Topp, G. Farahi, S. Klemenzenz, T. Gao, F. Rodolakis, J. L. McChesney, C. R. Ast, A. Yazdani, K. S. Burch, S. Wu, N. P. Ong, and L. M. Schoop, High mobility in a van der Waals layered antiferromagnetic metal, *Sci. Adv.* **6**, eaay6407 (2020).
- [19] Y. Iyeyiri, T. Okumura, C. Michioka, and K. Suzuki, Magnetic properties of rare-earth metal tritellurides $R\text{Te}_3$ ($R = \text{Ce, Pr, Nd, Gd, Dy}$), *Phys. Rev. B* **67**, 144417 (2003).
- [20] A. Raghavan, M. Romanelli, J. May-Mann, A. Aishwarya, L. Aggarwal, A. G. Singh, M. D. Bachmann, L. M. Schoop, E. Fradkin, I. R. Fisher, and V. Madhavan, Atomic-scale visualization of a cascade of magnetic orders in the layered antiferromagnet GdTe_3 , *npj Quantum Mater.* **9**, 47 (2024).
- [21] K. Deguchi, T. Okada, G. Chen, S. Ban, N. Aso, and N. Sato, Magnetic order of rare-earth tritelluride CeTe_3 at low temperature, in *Journal of Physics: Conference Series*, Vol. 150 (IOP Publishing, 2009) p. 042023.
- [22] J. Hamlin, D. Zocco, T. Sayles, M. Maple, J.-H. Chu, and I. Fisher, Pressure-Induced Superconducting Phase in the Charge-Density-Wave Compound Terbium Tritelluride, *Phys. Rev. Lett.* **102**, 177002 (2009).
- [23] D. A. Zocco, J. J. Hamlin, K. Grube, J.-H. Chu, H.-H. Kuo, I. R. Fisher, and M. B. Maple, Pressure dependence of the charge-density-wave and superconducting states in GdTe_3 , TbTe_3 , and DyTe_3 , *Phys. Rev. B* **91**, 205114 (2015).
- [24] More specifically, DyTe_3 has a double- \mathbf{q} charge ordering transition around $T_{\text{CDW,b}} = 50 \text{ K}$, but the strength of this order parameter is expected to be weak as compared to the predominant CDW-1 order parameter. (.)
- [25] S. Akatsuka, S. Esser, S. Okumura, R. Yambe, R. Yamada, M. M. Hirschmann, S. Aji, J. S. White, S. Gao, Y. Onuki, T.-h. Arima, T. Nakajima, and M. Hirschberger, Non-coplanar helimagnetism in the layered van-der-Waals metal DyTe_3 , *Nat. Commun.* **15**, 4291 (2024).
- [26] I. Shamova, J.-Y. Sun, X.-Y. Chang, V. Popova, D. Chareev, L. Shvanskaya, D. Ksenofontov, A. Vorobyova, K. Lyssenko, A. Demidov, H.-Y. Yeh, W.-Y. Tzeng, J.-Y. Lin, C.-W. Luo, P. Monceau, E. Pachaud, E. Lorenzo, A. Sinchenko, A. Vasiliev, and O. Volkova, Comparative study of terbium tellurides Tb_2Te_5 and TbTe_3 , *Phys. Rev. B* **112**, 094434 (2025).
- [27] S. Chillal, E. Schierle, E. Weschke, F. Yokaichiya, J.-U. Hoffmann, O. S. Volkova, A. N. Vasiliev, A. A. Sinchenko, P. Lejay, A. Hadj-Azzem, P. Monceau, and B. Lake, Strongly coupled charge, orbital, and spin order in TbTe_3 , *Phys. Rev. B* **102**, 241110 (2020).
- [28] In fact, Te_B includes two distinct crystallographic Wyckoff sites with same site symmetry and multiplicity. (.)
- [29] See Supplementary Information at (URL to be inserted by publisher).
- [30] R. Okuma, D. Ueta, S. Kuniyoshi, Y. Fujisawa, B. Smith, C. H. Hsu, Y. Inagaki, W. Si, T. Kawae, H. Lin, F. C. Chuang, T. Masuda, R. Kobayashi, and Y. Okada, Fermionic order by disorder in a van der Waals antiferromagnet, *Sci. Rep.* **10**, 15311 (2020).
- [31] M. Hanai, R. Ishikawa, M. Kawamura, M. Ohnishi, N. Takenaka, K. Nakamura, D. Matsumura, S. Fujikawa, H. Sakamoto, Y. Ochiai, T. Okane, S.-I. Kuroki, A. Yamada, T. Suzumura, K. Taura, Y. Mita, N. Shibata, and

Y. Ikuhara, ARIM-mdx Data System: Towards a Nationwide Data Platform for Materials Science, in *Pro-*

ceedings of 2024 IEEE International Conference on Big Data (BigData) (2024) pp. 2326–2333.